CFD ANALYSIS OF A MICRO-ROTOR IN GROUND EFFECT

Federico Rovere, [1] George N. Barakos, [2] René Steijl [3]
CFD Laboratory, School of Engineering, University of Glasgow, G12 8QQ, U.K.
www.gla.ac.uk/cfd

Abstract

In this work, computational fluid dynamics is used to compare experimental results for a two-bladed small rotor Out of Ground Effect and In Ground Effect conditions. The paper focuses on the evaluation and prediction of the performance of the rotor and investigates the outwash generated in ground effect. Time and phase averaged outflow velocities with two different scaling methods are compared with experiments. The results are also scaled to a full-size rotor, and compared with the PAXman model of crew operating in close rotor proximity. A particle pickup model is also used showing the dust cloud generated by the rotor.

Nomenclature

Acronyms

CFD	Computational Fluid Dynamics
DVE	Degraded Visual Environment
IGE	In Ground Effect
$MTOW$	Maximum TakeOff Weight
$MUSCL$	Monotone Upstream Centred Schemes for Conservation Laws
OGE	Out of Ground Effect
PIV	Particle Image Velocimetry

Greek

ν	Kinematic viscosity, m^2/s
Ω	Rotor angular velocity, rad/s
Ψ	Local azimuth angle, deg
ρ	Density, kg/m^3
τ_w	Wall shear stress, kg/ms^2
θ	Collective pitch at three-quarter radius, deg

Latin

a	Speed of sound, m/s
c	Blade chord, m
C_Q	Rotor torque coefficient, $C_Q = \frac{Q}{\frac{1}{2}\rho_\infty V_{tip}^2 \pi R^3}$
C_T	Thrust coefficient, $C_T = \frac{T}{\frac{1}{2}\rho_\infty V_{tip}^2 A}$
D	Rotor diameter, m
d_p	Particle diameter, μm
dF_{PAXman}	$dF_{PAXman} = \frac{1}{2}\rho V_{rad}^2 dA$, N
F_{PAXman}	$F_{PAXman} = \int_{A_{PAXman}} df_{PAXman}$, N
FoM	Figure of merit, $FoM = \frac{C_T^{3/2}}{2C_Q}$
g	Gravitional acceleration, m/s^2
h_{PAXman}	PAXman height scaled, m
M	Mach number, $M = V_{tip}c/a_\infty$
N_b	Number of blades
Q	Rotor torque, $N \cdot m$

[1]PhD Student - federico.rovere@glasgow.ac.uk
[2]Professor - george.barakos@glasgow.ac.uk - corresponding author
[3]Senior Lecturer - rene.steijl@glasgow.ac.uk

R	Rotor radius, m
r	Radial coordinate along blade span, m
Re	Reynolds number, $Re = V_{tip}c/\nu_\infty$
S_{rotor}	Rotor disk area, m^2
T	Rotor thrust, N
U	Velocity x-component, m/s
u^*	Friction velocity, m/s
V	Velocity y-component, m/s
v_i	Hover induced velocity, $v_i = \frac{\sqrt{(C_T)}}{2}$
v_{max}	Highest value of velocity radial component
V_{rad}	Velocity radial component, $V_{rad} = Ucos(\Psi) + Vsin(\Psi), m/s$

Super and sub scripts

∞	Freestream value
p	Particle
tip	Blade tip value

1   INTRODUCTION

The influence of the ground on the flowfield generated by a lifting rotor has been discussed in several works, using from full-scale aircraft [1] to small, isolated, rotors [2], [3] and [4]. This interaction between the flowflield and the ground changes the direction of the induced flow from vertical (downwash) to radial flow (outwash). Rotors operating In Ground Effect (IGE) may generate a dangerous environment for ground personnel, equipment, landscape and in case of brown-out or white-out for the aircrew too. To improve the safety of IGE operations the outflow of different aircraft has been measured and studied, (see [1] and [5]). The outwash flowfield has time-averaged characteristics similar to those of a wall-impinging jet [6] and its complexity is due to the persistence of the tip vortices and the interactions between rotors, airframe and ground plane. The ground interference also influences rotor performance. It decreases the power for a given thrust coefficient, and increases the thrust for a fixed amount of power. In the present work, computational fluid dynamics (CFD) analysis of a micro two-bladed rotor is compared with experimental results of the University of Maryland. A small rotor has been experimentally investigated for OGE and IGE in different configurations, and Ramasamy et al. [7] collected performance and flowfield data for OGE. In [8] the same small two-bladed rotor operating parallel to a ground plane at different heights was used. In both works, rotor performance was measured using a micro mass balance while the flowfield data was obtained by

2D Particle Image Velocimetry (PIV). In the present work, the CFD analysis has been validated based on results from these works [7] and [8]. The OGE validation is mainly focused on performance and visualization of the wake, while for the IGE test case the outflow is studied in detail. All CFD simulations have been performed using HMB3 (Helicopter Multi-Block) CFD solver. Initial results were obtained for the rotor OGE, and with a rotor one radius above the ground plane. Using the flowfield solutions, it is possible to evaluate several safety considerations to define a restricted zone around the rotor where the ouflow can be dangerous in terms of forces exercised on the people in proximity to the rotor, and in terms of uplifted particles. Safety separation distances already exist for wake encounters, and the Manual of Traffic Service [9] suggests a three-rotor-diameter separation distance. A detailed analysis on wake encounters was reported in [10], and this criterion can be used as a starting point to define a similar safety distance criteria for ground operations. Another source of danger due to the outflow is the presence in the flowfield of particles uplifted from the ground. During brown-out and white-out a cloud of particles (sand in the case of brown-out and snow for white-out) is generated, which may affect visibility.

2   CFD SOLVER

The HMB3 (Helicopter Multi-Block) [11] [12] is the solver used for all CFD calculations in this work. It solves the Unsteady Reynolds Averaged Navier-Stokes equations (URANS) in integral form with ALE formulation (Arbitrary Lagrangian Eulerian) formulation for time-dipendent domains (moving boundaries). URANS equations are discretised using a cell-centred finite volume approach on a multiblock structured grid. HMB3 uses the Osher [13] and Roe [14] approximate Riemann solvers to evaluate the convective fluxes, the viscous terms are discretized using second order central differencing. Third order accuracy in space is provided by The Monotone Upstream Centred Schemes for Conservation Laws (MUSCL) [15]. An implicit dual time stepping method is employed to perform the temporal integration. Oversets grids (used in this work) [16] and sliding plane [17] methods are available in HMB3 to allow for the relative motion between mesh components, representing ground and rotor blade. To avoid non-physical spurious oscillations HMB3 solves uses the alternative form of the Albada limiter [18] where large gradients are involved in computations, like in presence of shockwaves. Various turbulence models are available in HMB3, including one-equation, two-equation, three and four equations turbulent models. Large-eddy Simulation (LES), Detached-Eddy Simulation (DES) and Delay-Detached-Eddy Simulation (DDES) can also be used with HMB3. For this study two different turbulence model have been used: $k - \omega$ and $k - \omega$ SST [19], fur-

thermore due to the low Reynolds numbers of the test cases few laminar simulations were also performed.

2.1 PAXman MODEL

The PAXman model was developed for military personnel as a reference area for the wind force calculation, it is based on the projection of a crouching 6 ft tall person immersed in the outwash. The geometry of the PAXman model has been described in [1] and [5], and shown in fig 1. In this work, the PAXman height is scaled with the rotor radius of a UH-60A aircraft (R=8.18m), giving a height of $h_{PAXman} = 0.2R$. Using the reference area expressed by the polynomial representation of fig 1, it is possible calculate the distribution of the force produced by the outwash on the ground personnel. The forces are calculated as proposed in [1]. To obtain comparable forces with the safety criteria, velocities are scaled using the blade tip velocity of the UH-60A ($V_{tip} = 220$ m/s). In this way, it was possible to evaluate where the force due to the outflow reaches the safety threshold. However, the scaling in velocity cannot give an accurate rappresentation of reality, considering the UH-60A at max takeoff weight of MTOW=10,600kg, its rotor disk area of 210 m^2 and a tip velocity of 220 m/s it is possibile compute a realistic thrust coefficient using:

$$(1) \qquad C_T = \frac{2W_{MTOW}g}{\rho V_{tip}^2 S_{rotor}}.$$

The obtained thrust coefficient is $C_T = 0.0167$, which is lower of the mean of the micro-rotor thrust coefficient simulated in this work. However, for safety , the study of a rotor at higher thrust coefficient will lead to conservative safety criteria. According to [1] and [5] the caution zone begins when the force acting on the PAXman is more than 80 lbf (335 N), and the hazard zone is defined after 115 lbf (510 N). However in [5], there are not any specific instructions for operations in the "caution" or the "hazard" zones. In other words, these references do not define any safety constrains based on computed forces for people that are operating near the rotor. The distribution of the force over the body is calculated as: $f_{paxman} = \frac{1}{2}\rho V_{rad}^2 x$ where ρ is density the of the air, V_{rad} is the radial outflow velocity, and x is the horizontal coordinate of the PAXman model. The total force is the integral of the distribution of the force over the height of the PAXman model (z-component).

$$(2) \qquad F_{paxman} = \int_{h_{PAXman}} f_{paxman} dz$$

Using this model it is possible to calculate the force distribution acting on a human body at a specific radial station.

2.2 PARTICLE UPLIFT

A key element in the simulation of brown-out is the model used to represent the uplift of ground particles. For brown-out simulations the most popular uplift model is by Bagnold (see [20] and [21]) and simulates the pickup of particles in rivers or in aeolian flows. According to this model, a particle is aerodynamically entrained in the fluid flow if $u^* > u_t^*$, where $u^* = \sqrt{\tau_w/\rho_{air}}$ (τ_w being the wall shear stress) is the friction velocity and

$$(3) \qquad u_t^* = \sqrt{A(\frac{\rho_p}{\rho_{air}}gd_p + \frac{\beta}{\rho_{air}d_p})},$$

where u_t^* is the threshold velocity, while A and β are coefficients: A=0.0123 β=3e-04 $\frac{kg}{s^2}$

Another cause of particle uplift is "splash entrainment". Anytime an entrained particle hits the ground, it may have sufficiently high energy to launch more particles. The kinetic energy gained by the hit particles can overcome the cohesive forces and lead uplift. This phenomenon has not been taken into account in the present simulations, but it is described in [22] and [23].

2.3 PARTICLE TRACKING

The presence in the flowfield of particles may lead to dangerous situations like, as already said, brown-out and white-out. However other kind of particles, and even small stones can be uplifted by the wake. To properly simulate the behaviour of these in the flowfield it is necessary to model their motion. Lagrangian and Eulerian modelling are the two approaches used in the numerical simulation of particle motion in the flowfield. The Lagrangian approach has been used in [24] and [25]. In this approach the particles (or parcels of particles) are tracked through the field and the local cloud properties are defined by their properties as they pass each point in the space. In this approach, the motion of the particles is computing using the Newton's second law. In the Eulerian approach, the properties of the particles are assumed to be continuous within the flowfield. Thus, differential conservation equations are written, discredited, and solved for the properties of the cloud, e.g. [26] and [27]. For particle tracking, the commercial software Tecplot^{TM} has been used, and the motions of the particles follow a Lagrangian reference. The particles are driven by the flowfield velocities and their position in time are obtained by integrating their equation of motion, the particles are assumed massless. The integration method used is a second order Runge-Kutta , and the equation of motion for massless particles is:

$$(4) \qquad \boldsymbol{x}_p = (\boldsymbol{x}_{p0} + \boldsymbol{u}t)$$

Where $\boldsymbol{x}_p$ is the actual position of the particle, $\boldsymbol{x}_{p0}$ is its initial position, $\boldsymbol{u}$ is the velocity of the flowfield in the position of the particle and t is the time.

3 CFD COMPUTATIONS

3.1 OGE SIMULATIONS - RESULTS

The OGE test case has been analysed, and the characteristics of the two overset grids employed are presented in tab 2. The wake generated by the rotor is assumed to be steady. The hover configuration OGE can be seen as a steady problem at least before blade stall. The periodicity of the flow in the azimuthal direction allows modeling of only half of the domain (see fig 3 (a)). With minor changes, the blade geometry of [7] and [8] was replicated using ICEM hexa [28]. In particular, the blunt leading and trailing edges were rounded, but the differences in the modelled geometry are not expected to have any significant influence on the solutions. Two grids were generated to quantify mesh convergence. The coarse grid had approximately half the number of cells of the finer. Froude inflow and outflow have been imposed as reported in fig 3 (a). The "potential sink/Froude" boundary condition is used to suppress the re-circulation that arises from unperturbed free-stream far-field boundaries. The results obtained in terms of thrust, torque coefficient and figure of merit are shown in fig 4. Several simulations have been tested involving different turbulence models, different configurations and different Reynolds numbers. In [7], the authors, defined a scatter cloud and considered different types of blades at different collective angles. CFD results in terms of thrust and torque, generally underestimated the experimental results for the collective and Reynolds number proposed. However, the CFD results had the same trend as the experiments. The difference between the CFD and the experiment results is comparable to the difference between the different configurations of tested blades (presence of twist, taper and sharp leading and trailing edge), and this behaviour is probably due to the low Reynolds numbers used for simulations and experiment. In this configuration, extended separation zones are present on the blade, and the shape of the blade (in terms of airfoil and plane shape) loses part of its influence on performance. For this reason, no more blade configurations were taken into account for CFD validation than the baseline. The simulated flowfield contains the typical behaviour shown in experiments with PIV. Tip vortices, and vortex sheets are clearly visible and comparable with the observed flowfield of reference [8]. In fig 6 lift and drag are compared per unit of span. In general, for both forces the agreement is good. However, the drag is overesistimated starting from y/R=08. In [7], lift and the drag were computed along the blade from the data extracted from the PIV, but due to the small size of the blade it was not possible use pressure sensors. The lift was computed from the bound circulation at different stations, while the drag was extracted evaluating the loss of momentum behind the blade. The CFD results for lift have been computed in two ways, from the

circulation (the same as the experiment) and from the blade pressure data. The pressure-based lift has a peak near the tip, that the circulation-based lift (from experiments and CFD) did not show. This can be due to 3D effects due to the tip vortex in proximity of the tip. This effect have a minimum interference on the 2D bound circulation, however, it can have a stronger effect on the pressure tip.

3.2 IGE SIMULATIONS - RESULTS

For the IGE configuration, the rotor was modelled using two overset grids, and no-slip and no-penetration conditions were imposed on the ground. The rotor domain was computed as unsteady, for the IGE case. The unsteady time step was changed during the simulation. The first two revolutions have computed at 5deg/timestep. Then, the timestep was gradually reduced reaching 0.5deg/timestep for the last revolutions performed. The mesh has been refined near the ground and the rotor to accurately resolve the wake features. Investigations were conducted analyzing the radial velocity at different distances from the rotor and comparing with experiments [8]. The results are shown as time-averaged and phase-averaged radial velocities, for two azimuth positions (Ψ=0 deg and Ψ=90 deg). Comparison in terms of performance are given in fig 7 (C_T^{IGE}/C_T^{OGE} and C_Q^{IGE}/C_Q^{OGE} ratios) and show small differences with of the experiments of [8]. For the CFD results, the influence of the ground appears to be weaker than in the experimental results. At similar thrust coefficients, the power required with the ground was higher for the CFD. However the thrust coefficient, shows a results close to the result proposed by Lee et al. [8]. The increment of thrust coefficient IGE is about 10% with respect to the OGE case. The result of the power coefficient is slightly higher than what expected C_Q^{IGE}/C_Q^{OGE}=1.02. However, it can be considered that the power between OGE and IGE is fairy constant, with a small incrementum in the thrust coefficient as expected. Similar results in terms of C_Q^{IGE}/C_Q^{OGE} have been obtained by Karla et al. in [29] for the same test case. In fig 5 the rotor wake is presented as (a) iso-surfaces of Q-criterion and (b) contours of vorticity magnitude. As expected, the wake, reaches the ground and expands. The time and phase-averaged velocity has been scaled using two different methods. First, the radial velocity is scaled with the reference hover induced velocity $v_h = \frac{\sqrt{(C_T)}}{2}$, which is a rotor parameter. The velocity is scaled as a jet, with v_{max}, to explore the self - similar characteristic of the wall jet. The dashed line shown in the figs 9 and 10 represents the PAXman model height.

The time averaged velocities show good agreement with experiments in terms of maximum radial velocity near the rotor as, figs 9 (a) and (c) suggest. For higher radial positions (about $r/R = 2$) the peak velocity is un-

derestimated (fig 9 (e)) . This could be due to a different distribution of the momentum between the rotor and the ground. It can be noticed that where the peak is underestimated, the full distribution of the outflow shows a different behaviour. This can be due to the small number of revolutions performed. CFD results are obtained after 4 full rotor revolutions, due to the high computational cost of the simulations. This may not allow the flowfield to develop properly far from the rotor. Phase averaged results are shown in fig 10. Here, the solid lines represent the experimental results in [8], while the dashed line shows the CFD results from this work. Different colours are used for different azimuth position (red lines for azimuth $\Psi = 0$ deg, blue lines for Ψ =90 deg), solid and dashed line with the same colour are compared. figs 10 (a) and (b) show good agreement and suggest strong velocity fluctuations. In fig 10 (c) the peak is underestimated as in the case of time average results. However, the phase-averaged outflow at Ψ=90 deg is not far from the experimental results, while the case of Ψ=0 deg is more in agreement with the time-averaged results. At this radial position, it was expected to see a more settled outflow with comparable outflow at different azimuth angles. However the outflow shows fluctuations between different phases. Perhaps the simulations have to be performed for more revolutions to obtain a well settle flowfield at larger distances.

3.3 SAFETY CONSIDERATIONS

Fig 13 (a) shows the total forces acting on a scaled human body at different distances by the outflow produced by the rotor. The forces have been computed scaling the velocities with the UH-60A V_{tip} of 220 m/s, to obtain more realistic values and compare them with the safety thresholds suggested for civilian and military operations. The forces are stronger at radial distances of 1.25 and 1.5R, and for larger distances they weaken. This agrees with the outflow results discussed earlier. The highest velocities are seen near 1.5R. It is clear that the area near the rotor (between 1R and 1.75R is the most dangerous). Here, the forces exceed the limits of caution and danger. The peak force was 600 N. In [5], similar results have been obtained for a V-22 where the hazard zone can be identified between 1 and 2R, with peaks around 620 N for certain configurations. The model rotor used for the experiment had a $C_T = 0.03$, which is a high value for a real rotor. Such value of C_T can produce strong downwash and outwash velocities if scaled to a fullscale V_{tip} like the one used in this work. In this case, the computed forces are overestimated respect to a real full scale case, so the safety considerations performed are conservative. Futhermore, in [1] consider the influence of the disk loading and the hover height as parameters that have effects on PAXman forces, in this work only a single configuration has been considered. After 2R, the force drops quickly, and this is due to the outflow velocities that drops fast away from the rotor. After a 3R distance the force is almost negligible for the PAXman model. Fig 13 (b) presents the distribution of the forces over the PAXman height. It can be noticed that at every radial station away from the rotor the force is strongest at a height corresponding to the PAXman chest. This result is due to the shape of the outwash distribution and the larger blocking area at chest level. This is also in agreement with other investigations. In [1] the force peaks were around the middle of the human body, however, the experiment performed by Silva et al., was at full scale.

Evaluating, the shear stress on the ground of the domain allows to calculate the particle velocity uplift threshold. The proprieties of the particles, listed in tab 4, chosen according to [23], that give some example values. Using the Bangold model, it is possible to obtain $u_t^* = 0.2534$ m/s. Keeping the original scaling factor, the uplift model has been calculated on the ground of the flowfield, and is shown in fig 11. It is possible to see how the uplift ratio u_t/u_t^* reaches a value greater than one in a defined zone of the flowfield. The uplifted particles define a circle of around 1R around the rotor. Here, the majority of the particles are uplifted and enter the flowfield. Using the UH-60 scaling velocity of $V_{tip} = 220$ m/s the situation is different as shown in fig 11 (b) .The ratio reaches higher values, and all particles inside an area of 2.5R around the rotor can be uplifted. Fig 12 shows the influence of the starting vortex on the uplift model. Vorticity magnitude shows the presence of the starting and the tip vortices in the wake. It can be noticed that the highest value of uplift ratio in the area of the outer vortex.

Using these data it was possible to seed properly the ground where the particles are more affected by the flowfield. Fig 14 shows the evolution of the particles in time. This calculation spans 4000 revolutions, for a total time of 15 minutes (enough for a short operation near ground). The velocity involved in the flowfield generated by the tested model rotor were not able to lift particles. To obtain more realistic results the flowfield has been scaled using a possible operational V_{tip} of the UH-60A helicopter (220 m/s). Initially, the particles are uplifted, and they move away from the rotor along the radial direction. Particles are driven by the outflow that pushes them away from the rotor, but after a certain distance (around 7R) the outflow loses its strength, and particles are uplifted and reingested in the flow. Uplifted particles can reach more than 3R height. This identifies a zone with presence of particles (inside 7R) and a zone without particles. The 3 rotor diameters criterion used in wake encounters [9], [10] can be seen to overlap with PAXman criterion (PAXman forces are negligible after 3R). However, due to the results obtained, the presence of particles inside the 3 diameters distance suggests that the distance criterion for wake encounters should be extended at least by 1 rotor diameter to exclude the presence of the particles in the flowfield. Particles that move away from the rotor can be dangerous for ground personnel and equipment, while the recirculation of the

particles creates risks for the helicopter and the crew itself. During the reingesting phase, particles can hit the blade and fuselage and create the cloud that spoils the view of the pilot, leading to the dangerous DVE conditions.

4 CONCLUSION AND FUTURE STEPS

CFD results are seen to be in fair agreement with the experimental data in terms of rotor performance for OGE and IGE rotors, even if a slightly higher torque is seen in IGE case. However, there were some differences in the outflow predictions for IGE, and in particular at stations away from the rotor. These differences can be extremely important if used to evaluate safety criteria near the helicopter. The scaling factors lead to different levels of agreement with experiments, and only the scaling with the induced velocities gives a complete understanding of the outflow analysis in terms of safety. The normalized magnitude of the radial velocity peaks in the outflow, and its position, related to the PAXman model height, are fundamental to obtain correct force estimations. Typically, jet-scaled outflow shows better agreement with experiments, however, this gives information only about the momentum distribution at the level of the rotor, and can be used to emphasize which portions of the PAXman body are more influenced by the outflow. The IGE calculations show worst agreement at larger radial stations, and more effort need to understand these. Away from the rotor, the flowfield is less influenced by the instant fluctuations produced by the rotor, and its characteristics are mainly defined after a period of several revolutions. Safety considerations show that the distance criterion based on the PAXman forces and uplift of particles, can be deducted by the outflow analysis, and forces after 3R are low. So the wake encounter criterion of 3D [9], [10] can be adopted for ground operation, if the presence of particles on the ground can be excluded. Particle tracking results show that uplifted particles reach distances larger than 3D. Futher investigations should be carried out to include different configurations of rotors, hover heights, and disk loadings.

5 Acknowledgments

References

[1] Silva, M. and Riser, R., "CH-47D tandem rotor outwash survey," *AHS 67th Annual Forum*, 2011.

[2] Curtiss, H., Sun, M., Putman, W., and Hanker, E., "Rotor aerodynamics in ground effect at low advance ratios," *Journal of the American Helicopter Society*, Vol. 29, No. 1, 1984, pp. 48–55.

[3] Rauleder, J. and Leishman, J. G., "Flow Environment and Organized Turbulence Structures Near a Plane Below a Rotor," *AIAA journal*, Vol. 52, No. 1, 2014, pp. 146–161.

[4] MilluzzoIII, J. I. and Leishman, J. G., "Vortical sheet behavior in the wake of a rotor in ground effect," *AIAA Journal*, Vol. 55, No. 1, 2016, pp. 24.

[5] Preston, J. R., Troutman, S., Keen, E., Silva, M., Whitman, N., Calvert, M., Cardamone, M., Moulton, M., and Ferguson, S. W., "Rotorwash Operational Footprint Modeling," Tech. rep., Missile research development and engineering center redston arsenal al missile guidance directorate, 2014.

[6] Glauert, M., "The wall jet," *Journal of Fluid Mechanics*, Vol. 1, No. 6, 1956, pp. 625–643.

[7] Ramasamy, M., Johnson, B., and Leishman, J. G., "Understanding the Aerodynamic Efficiency of a Hovering Micro-Rotor," *Journal of the American Helicopter Society*, Vol. 53, No. 4, 2008, pp. 412–428.

[8] Lee, T. E., Leishman, J. G., and Ramasamy, M., "Fluid dynamics of interacting blade tip vortices with a ground plane," *Journal of the American Helicopter Society*, Vol. 55, No. 2, 2010, pp. 22005–22005.

[9] CAA, "CAP 490: Manual of Air Traffic Services Part 1," 2015.

[10] Jimenez-Garcia, A., Barakos, G., Treve, V., Rooseleer, F., Cappellazzo, V., and Graham, R., "Helicopter Wake Encounters in the Context of RECAT-EU," 2017.

[11] Steijl, R., Barakos, G., and Badcock, K., "A framework for CFD analysis of helicopter rotors in hover and forward flight," *International journal for numerical methods in fluids*, Vol. 51, No. 8, 2006, pp. 819–847.

[12] Lawson, S., Woodgate, M., Steijl, R., and Barakos, G., "High performance computing for challenging problems in computational fluid dynamics," *Progress in Aerospace Sciences*, Vol. 52, 2012, pp. 19–29.

[13] Osher, S. and Chakravarthy, S., "Upwind schemes and boundary conditions with applications to Euler

equations in general geometries," *Journal of Computational Physics*, Vol. 50, No. 3, 1983, pp. 447–481.

[14] Roe, P. L., "Approximate Riemann solvers, parameter vectors, and difference schemes," *Journal of computational physics*, Vol. 43, No. 2, 1981, pp. 357–372.

[15] Van Leer, B., "Towards the ultimate conservative difference scheme. V. A second-order sequel to Godunov's method," *Journal of computational Physics*, Vol. 32, No. 1, 1979, pp. 101–136.

[16] Jarkowski, M., Woodgate, M., Rokicki, J., and Barakos, G., "Towards consistent hybrid overset mesh methods for rotorcraft CFD," 2011.

[17] Steijl, R. and Barakos, G., "Sliding mesh algorithm for CFD analysis of helicopter rotor–fuselage aerodynamics," *International journal for numerical methods in fluids*, Vol. 58, No. 5, 2008, pp. 527–549.

[18] Van Albada, G., Van Leer, B., and Roberts, W., "A comparative study of computational methods in cosmic gas dynamics," *Upwind and High-Resolution Schemes*, Springer, 1997, pp. 95–103.

[19] Menter, F. R., "Two-equation eddy-viscosity turbulence models for engineering applications," *AIAA journal*, Vol. 32, No. 8, 1994, pp. 1598–1605.

[20] Bagnold, R., "The physics of blown sand and desert dunes. London: Methuen." 1941.

[21] Greeley, R. and Iversen, J. D., *Wind as a geological process: on Earth, Mars, Venus and Titan*, Vol. 4, CUP Archive, 1987.

[22] Shao, Y. and Li, A., "Numerical Modelling of Saltation in the Atmospheric Surface Layer," *Boundary-Layer Meteorology*, Vol. 91, No. 2, May 1999, pp. 199–225.

[23] Shao, Y. and Lu, H., "A simple expression for wind erosion threshold friction velocity," *Journal of Geophysical Research: Atmospheres*, Vol. 105, No. D17, 2000, pp. 22437–22443.

[24] Alfred, J., Celi, R., and Leishman, J. G., "Flight Path Optimization for Brownout Mitigation Using a High-Fidelity Simulation Model," *Journal of the American Helicopter Society*, Vol. 62, No. 3, 2017, pp. 1–15.

[25] Wachspress, D., Whitehouse, G., Keller, J., Yu, K., Gilmore, P., Dorsett, M., and McClure, K., "A high fidelity brownout model for real-time flight simulations and trainers," Vol. 1, 2009, pp. 278–301, cited By 27.

[26] Phillips, C., Kim, H. W., and Brown, R. E., "The flow physics of helicopter brownout," *66th American Helicopter Society Forum: Rising to New Heights in Vertical Lift Technology*, 2010.

[27] Ghosh, S., Lohry, M. W., and Rajagopalan, R. G., "Rotor configurational effect on rotorcraft brownout," *28th AIAA Applied Aerodynamics Conference*, 2010, p. 4238.

[28] ICEM CFD, "ver. 17.2," *ANSYS Inc., Southpointe*, 2017.

[29] Kalra, T. S., Lakshminarayan, V. K., and Baeder, J. D., "CFD validation of micro hovering rotor in ground effect," *American Helicopter Society 66th Annual Forum Proceedings*, Citeseer, 2010.
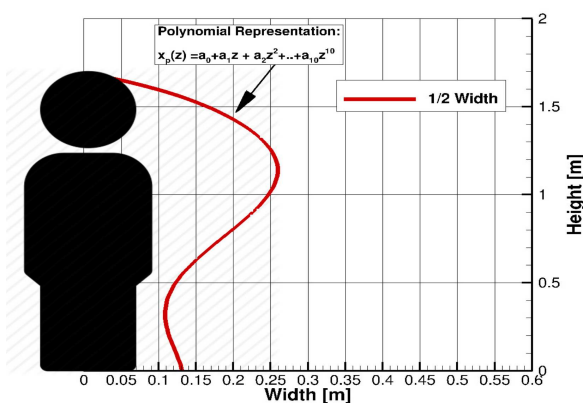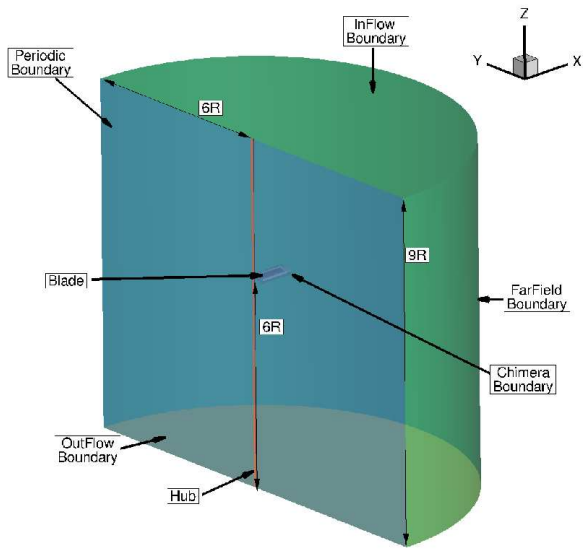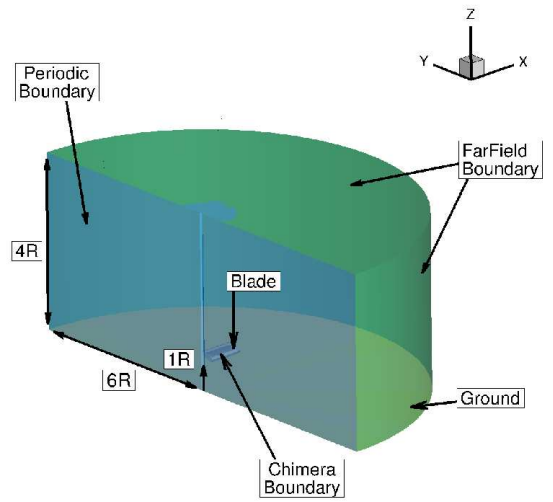
Figure 1: PAXman model [5]

a0	4.30939e-01
a1	-4.63972e-02
a2	-1.39649e-01
a3	1.37545e-01
a4	-2.48764e-02
a5	-5.49253e-04
a6	2.21653e-04
a7	-4.18444e-05
a8	1.45194e-05
a9	-7.80009e-08
a10	-1.89822e-07

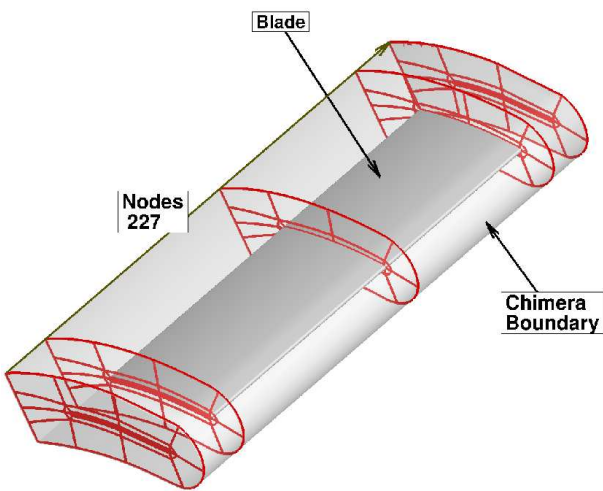Table 1: Polynomial coefficients used for the curve in fig 1.
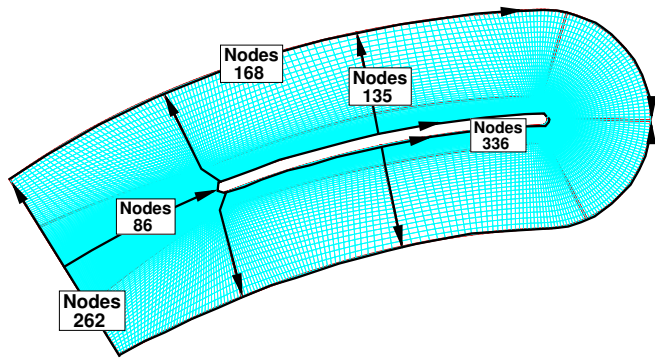
(a) OGE domain

(b) IGE domain

Figure 2: CFD domains and boundary conditions for the background for OGE and IGE calculations.

(a) blade

(b) airfoil

Figure 3: Foreground mesh used for the rotor blades [8] and [7].

Name	1	2	3	4	5	6
Grid Technique Component	Chimera Blade	Chimera Background	Chimera Composite	Chimera Blade	Chimera Background	Chimera Composite
Collective	0		12	0		0
N blades	1		2	1		2
Mesh component			1+2			4+5
Scaling factor	c	c	c	c	c	c
Dimension of the grid Number of points (Millions)	7.14 M	12.50 M	19.65 M	15.1 M	29 M	44.17 M
Distance from the ground Blade plane			3R			9R
Top domain			9R			9R
Side domain			6R			6R
Minimum distance	$1 \cdot 10^{-4}c$	$5 \cdot 10^{-4}c$	$5 \cdot 10^{-4}c$	$1 \cdot 10^{-5}c$	$5 \cdot 10^{-5}c$	$1 \cdot 10^{-5}c$

Table 2: CFD Grids for the Ramasamy et al. [7] test case.

Mesh	1	2	3	4	5	6	7
Grid Technique Component	Chimera Blade	Chimera BackGround	Chimera Composite	Chimera BackGround	Chimera Composite	Chimera Hub	Chimera Composite
Collective	0		12		12		12
N blades	1		2		2		2
Mesh component			1+1+2		1+1+4		1+1+4+6
Scaling factor	c	c	c	c	c	c	c
Number of Points (Millions) Distance from the ground	7.14 M	23.18 M	37.47 M	20.82 M	35.11 M	0.01 M	35.2 M
Blade plane			0.5R		1R	1R	1R
Top of domain			1R		1R	4R	4R
Side of domain			4R		4R	4R	6R

Table 3: CFD Grids for the Lee et al. [8] test case.

$\rho_p(kg/m^3)$	$d_p\,(\mu m)$	$u_t^*(m/s)$
2650	63	0.25
$\rho_{air}(kg/m^3)$	$\nu(m/s^2)$	$g(m/s^2)$
1.225	1.516	9.81

Table 4: Properties of ground particles used in this work, with air data [23].
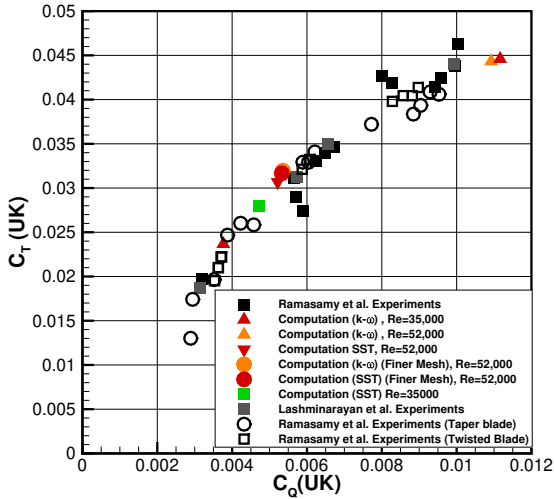
(a) C_T vs C_Q
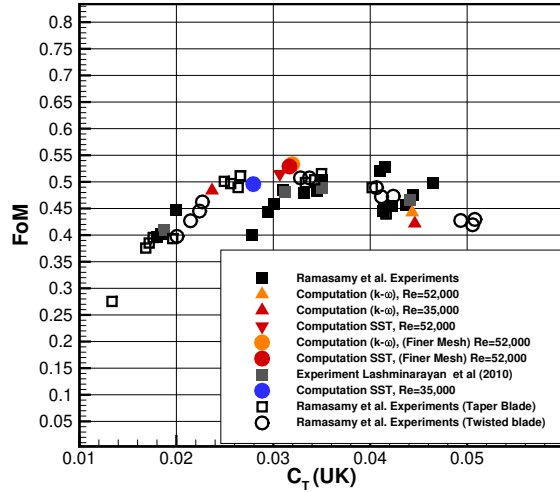
(b) FoM vs C_T

Figure 4: Experimental and CFD results for different OGE test cases. The rotor corresponds to the design reported in [7]. Tested at two different collective θ_{75}=12deg and θ_{75}=20deg, $M_{tip} = 0.082$. Reynolds number is based at tip flow conditions Re_{tip}.
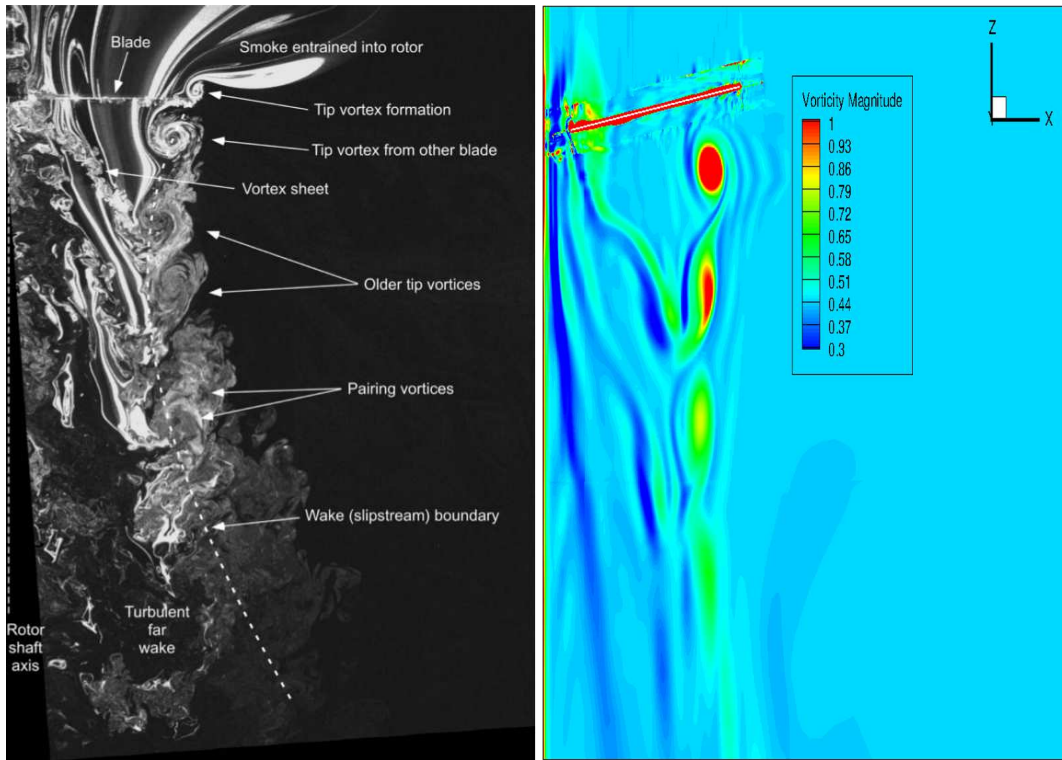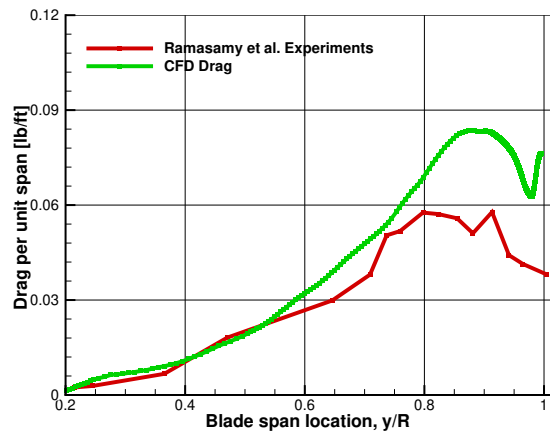

(a) Experimental [8]

(b) CFD

Figure 5: Experimental and CFD wake visualisation at OGE conditions The rotor corresponds to the design reported in [7], at collective $\theta_{75} = 12deg$, $Re_{tip} = 35000$ and $M_{tip} = 0.082$. The turbulent model $k - \omega$ was used for calculations.
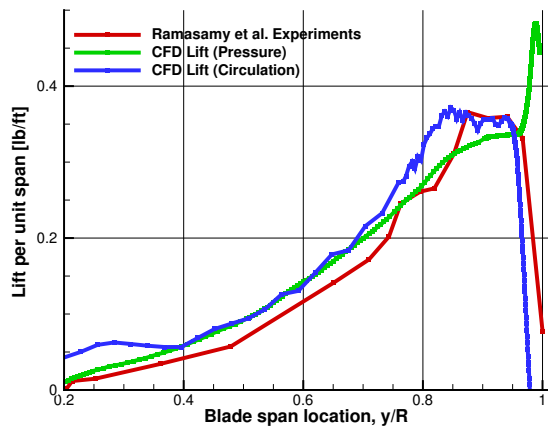
(a) Lift

(b) Drag

Figure 6: Experimental and CFD results for lift and drag distributions along the rotor blade. The rotor was operating OGE, at $Re_{tip} = 35000$, $\theta_{75} = 12deg$ and $M_{tip} = 0.082$. Experimental data was taken from [7].
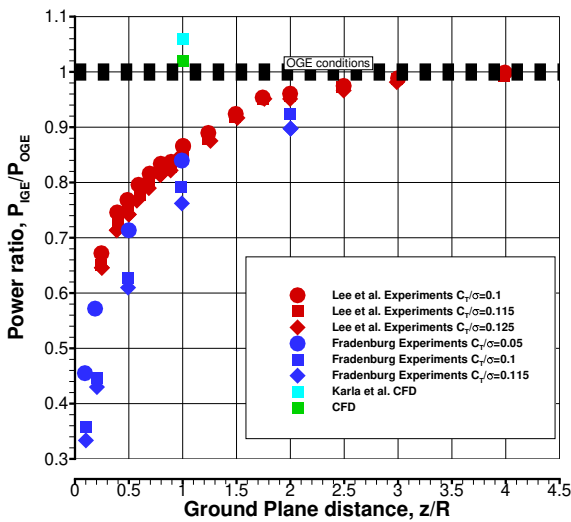
(a) $\frac{C_P^{IGE}}{C_P^{OGE}}$
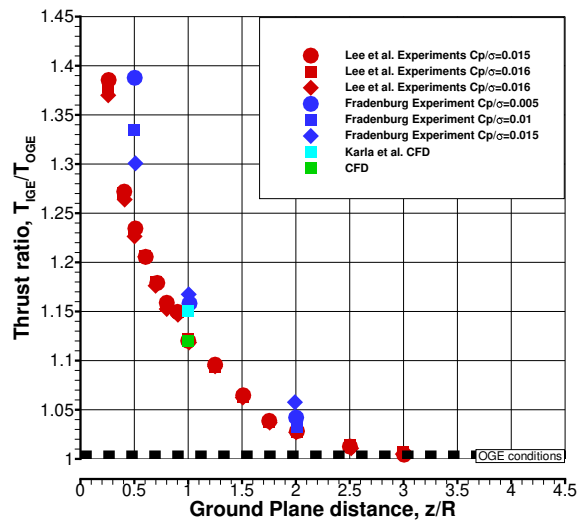
(b) $\frac{C_T^{IGE}}{C_T^{OGE}}$

Figure 7: Experimental and CFD results for the power and trust ratios IGE. The rotor was operating at $\theta_{75} = 12deg$, $Re_{tip} = 35000$ and $M_{tip} = 0.08$. Experimental data taken from [8] and additional CFD data from [29].

11

(a) Q criterion iso-surface

(b) Vorticity
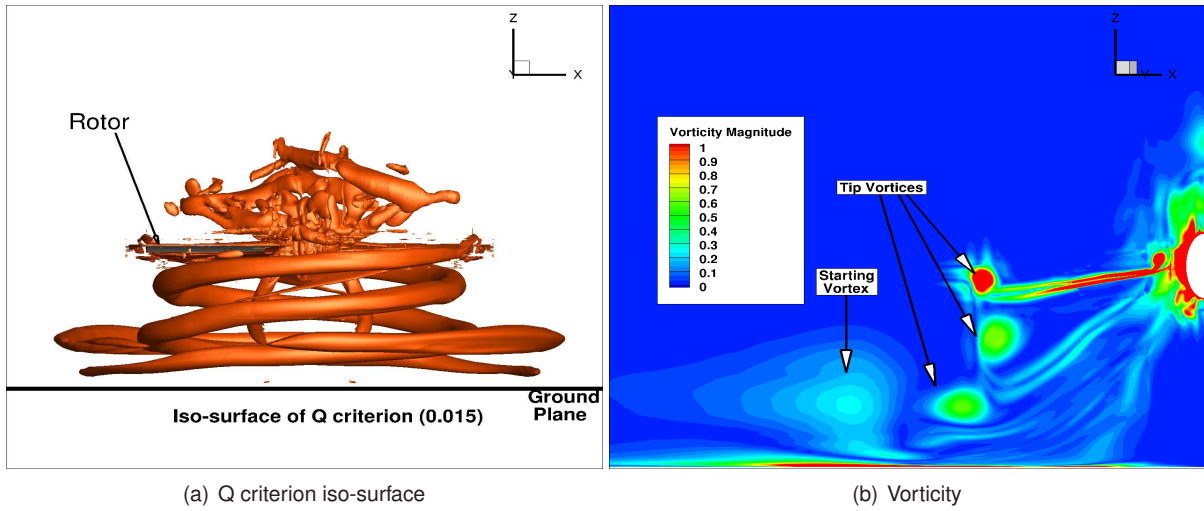
Figure 8: Wake Visualization, for the IGE case. The rotor operating at $\theta_{75} = 12deg$, $Re_{tip} = 35000$, $M_{tip} = 0.08$, $h/R = 1$ and $C_T = 0.03$.


(a) V_{rad}/v_i at r/R=0.8

(b) V_{rad}/v_{max} at r/R=0.8

(c) V_{rad}/v_i at r/R=1.0

(d) V_{rad}/v_{max} at r/R=1.0

(e) V_{rad}/v_i at r/R=2.0

(f) V_{rad}/v_{max} at r/R=2.0
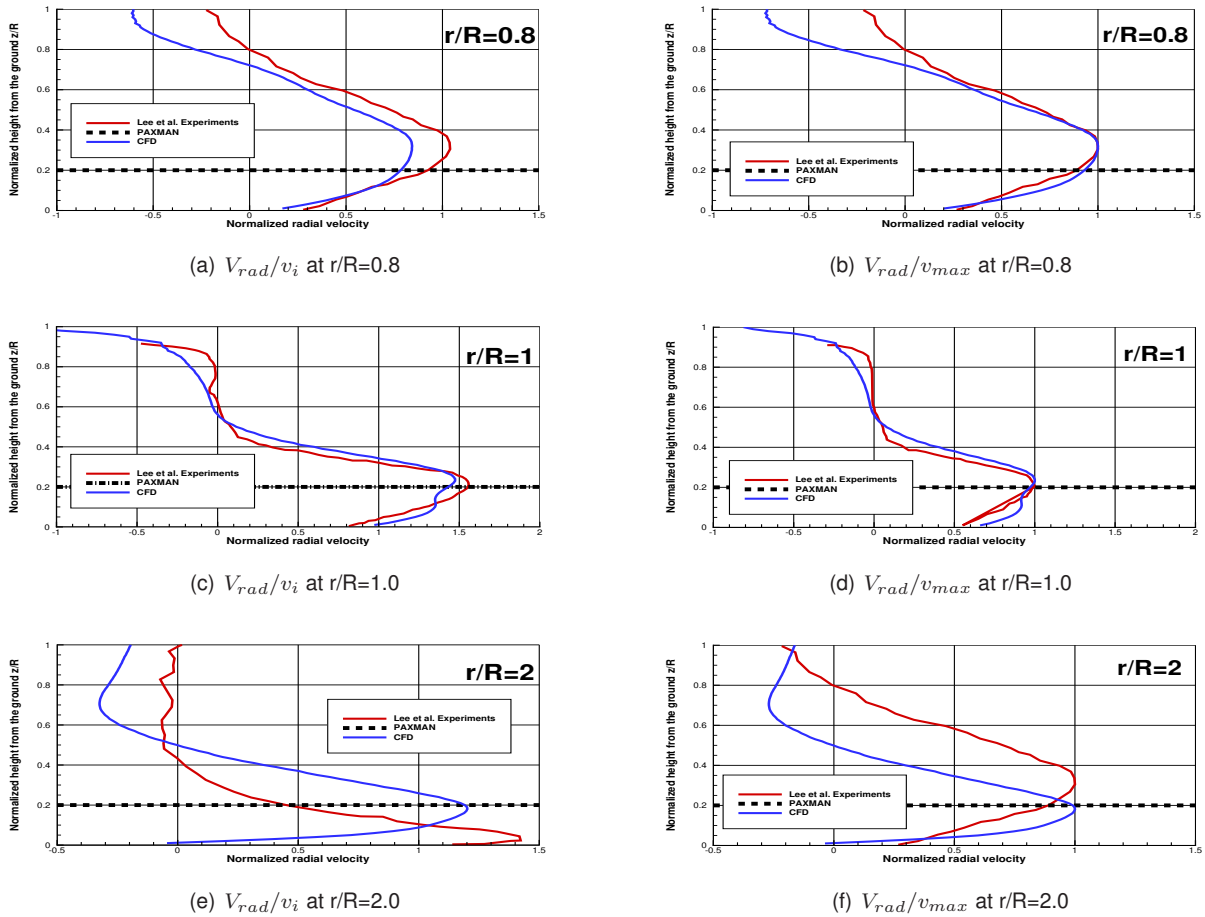
Figure 9: Experimental and CFD time-averaged outflow velocity profiles at different radial positions. The rotor was operating $\theta_{75} = 12deg$, $Re_{tip} = 35000$ $M_{tip} = 0.08$ and $C_T = 0.03$.. Left column results are scaled with induced hover velocity, while the right column results are scaled with jet-scaled velocity. Experimental data taken from [8].
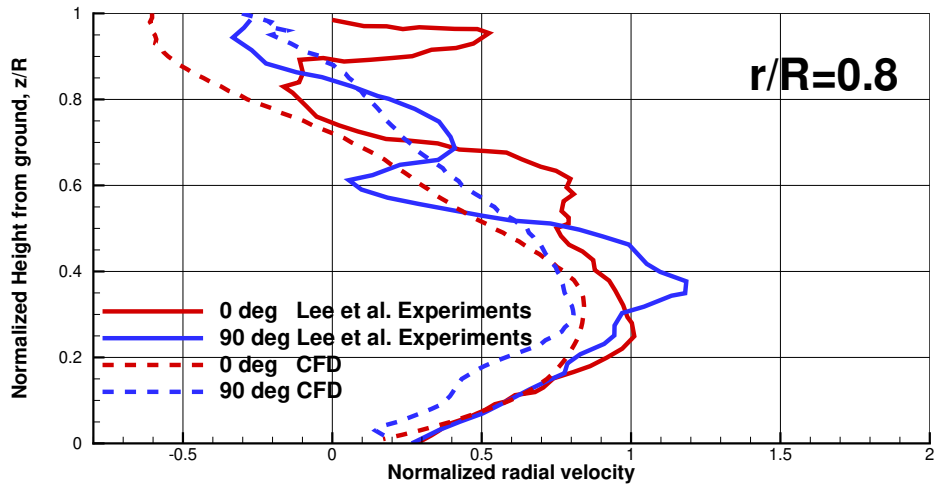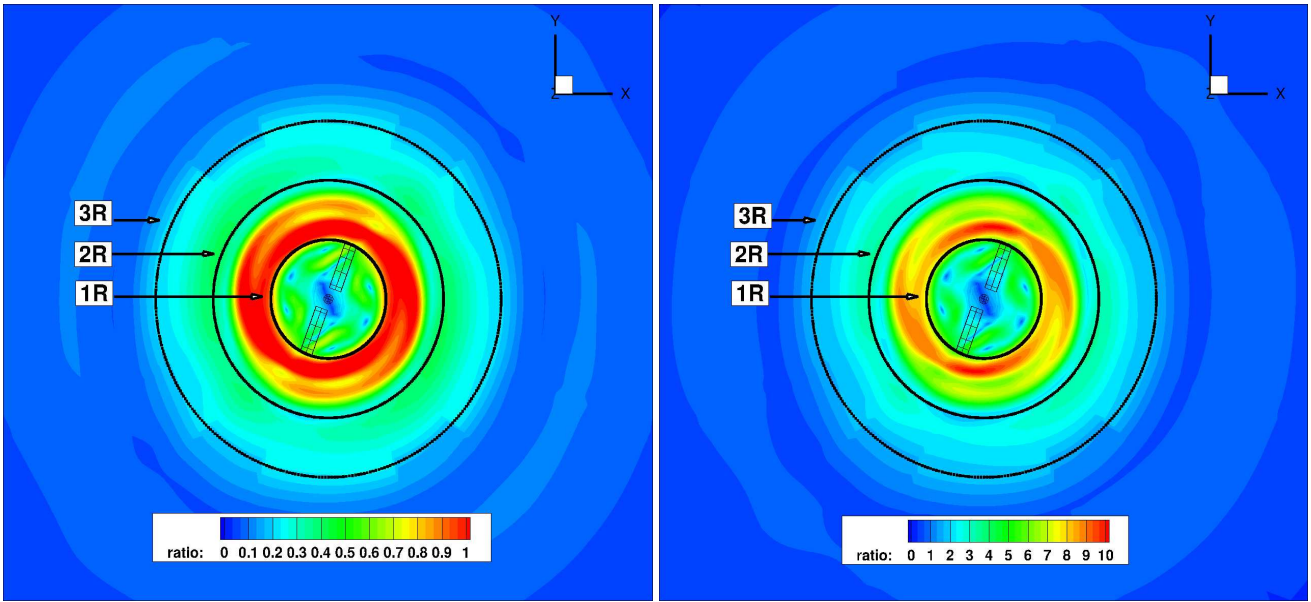
(a) r/R=0.8
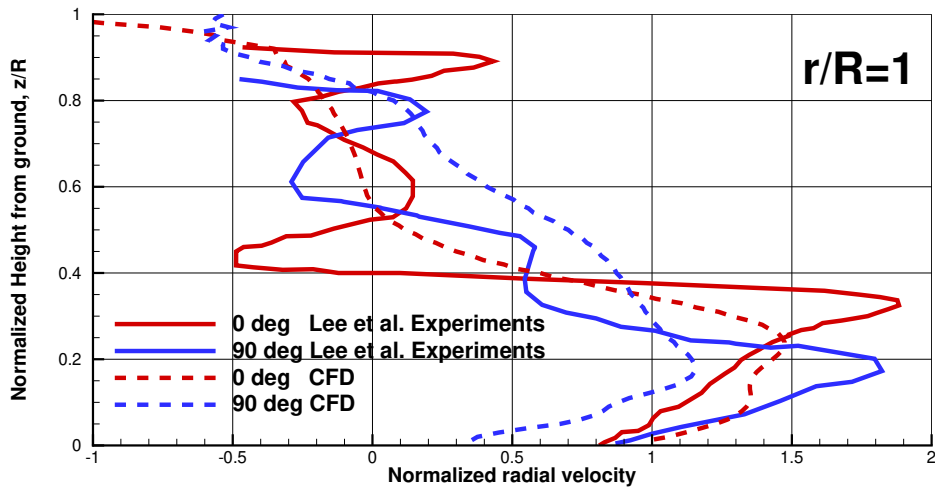
(b) r/R=1
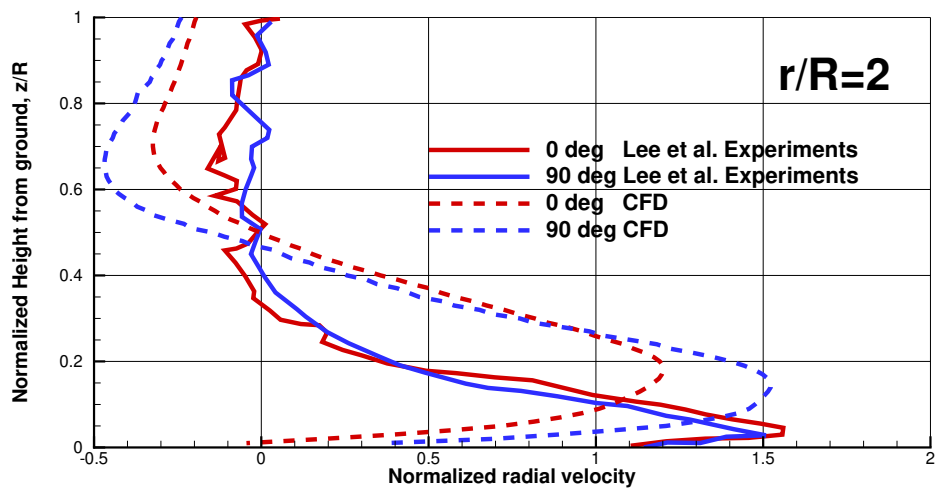
(c) r/R=2

Figure 10: Experimental and CFD phase-averaged velocity profiles V_{rad}/v_i at different radial positions and at azimuth angles. Ψ=0 and Ψ=90 deg. The rotor was operating $\theta_{75} = 12deg$, $Re_{tip} = 35000$, $M_{tip} = 0.08$ and $C_T = 0.03$. Experimental data taken from [8].

(a) $V_{tip} = 27$ m/s

(b) $V_{tip} = 220$ m/s

Figure 11: Uplift ratio $(\frac{u_t}{u_t^*})$ for particles with $u_t^* = 0.2534$ m/s. The rotor was operating at $\theta_{75} = 12deg$, $Re_{tip} = 35000$, $M_{tip} = 0.08$, $h/R = 1$ and $C_T = 0.03$.
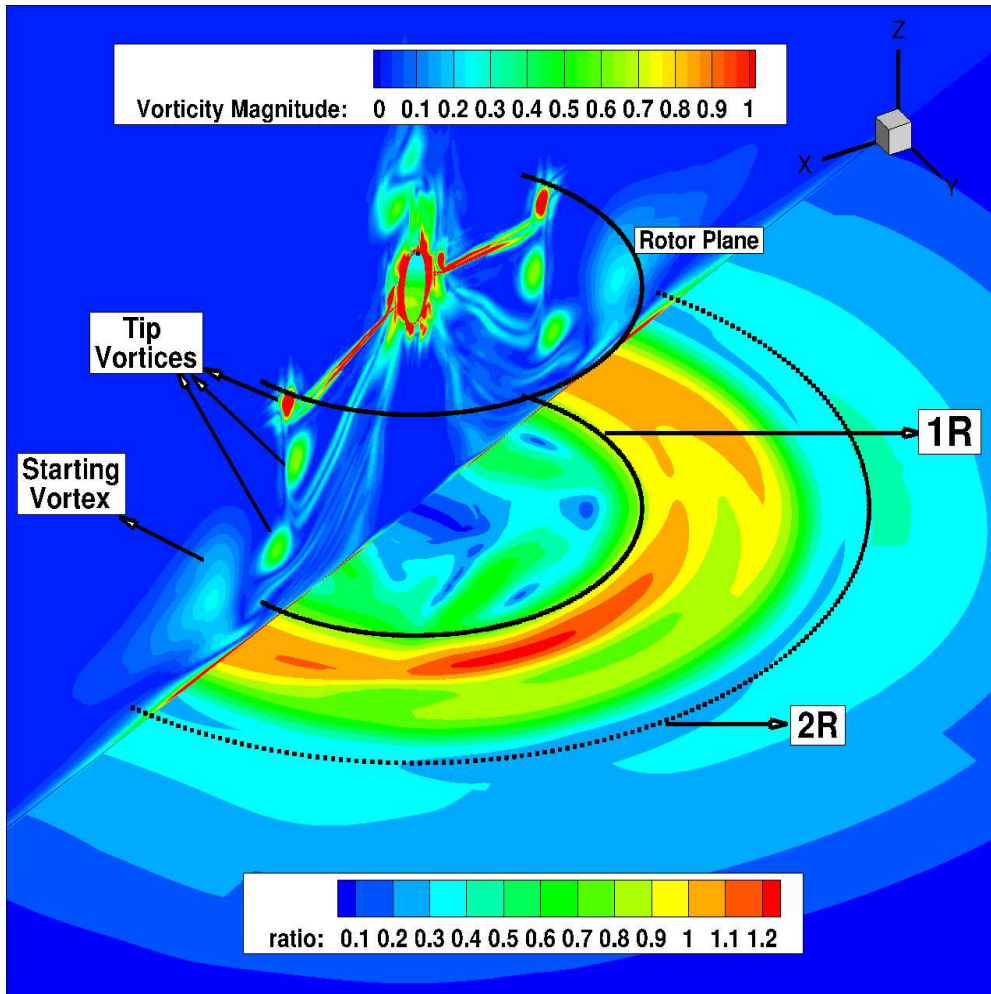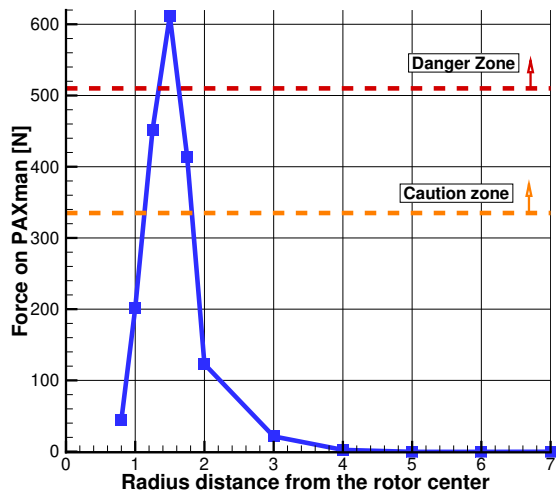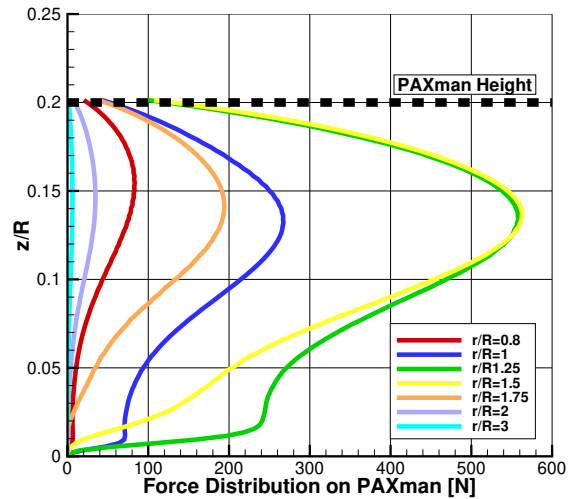

Figure 12: Uplift ratio $(\frac{u_t}{u_t^*})$ for particles with $u_t^* = 0.2534$ m/s, and vorticity magnitude. The rotor was operating at $\theta_{75} = 12deg$, $Re_{tip} = 35000$, $M_{tip} = 0.08$, $h/R = 1$ and $C_T = 0.03$.

14

(a) Total radial force F_{PAXman}

(b) Radial force distibution f_{PAXman}

Figure 13: PAXman model forces calculated using the employed micro-rotor, scaled to $V_{tip} = 220$ m/s. The rotor was operating at $\theta_{75} = 12deg$, $Re_{tip} = 35000$, $M_{tip} = 0.08$, $h/R = 1$ and $C_T = 0.03$.
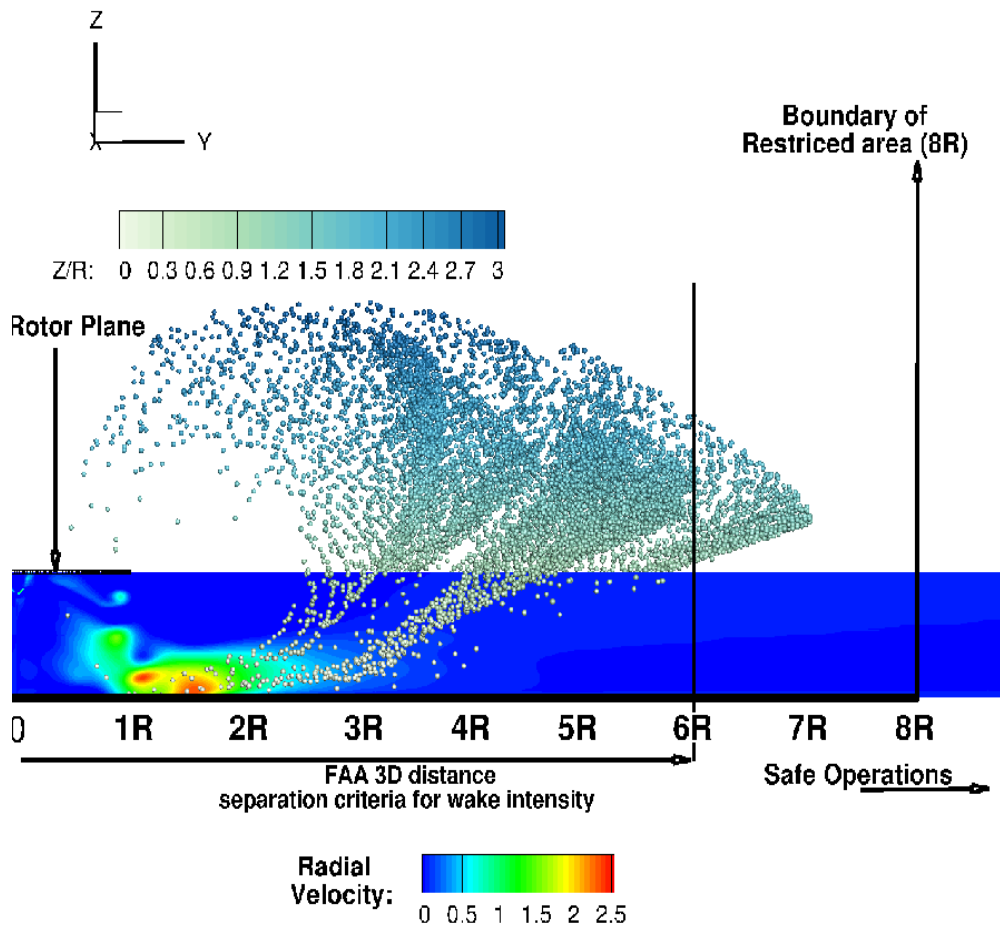

Figure 14: Particle tracking, using velocities scaled with th UH-60 tip velocity ($V_{tip} = 220$ m/s). Massless particle paths are calculated over a period of 15 minutes. The rotor was operating at $\theta_{75} = 12deg$, $Re_{tip} = 35000$, $M_{tip} = 0.08$, $h/R = 1$ and $C_T = 0.03$. Contours correspond to the radial velocity magnitude (V_{rad}) and the FAA 3 diameters separation distance is shown for comparison [9].